Microstructure Control of Zn/ZnO Core/Shell Nanoparticles and Their Temperature-Dependent Blue Emissions

Haibo Zeng,*,† Zhigang Li, Weiping Cai,*,‡ Bingqiang Cao, Peisheng Liu, and Shikuan Yang

Key Laboratory of Materials Physics, Anhui Key Laboratory of Nanomaterials and Nanostructure, Institute of Solid State Physics, Chinese Academy of Sciences, Hefei 230031, P.R. China

Received: September 1, 2007; In Final Form: October 7, 2007

The microstructure of the Zn/ZnO core/shell nanoparticles synthesized by laser ablation in liquid medium can be facilely controlled. With the surfactant concentration increased over the critical micelle concentration, the nanoparticle transformed from pure ZnO to a Zn/ZnO core/shell structure. Further, with a decrease of the applied laser power, the ZnO shell thickness was monotonously reduced till 2.5 nm and the ultrafine ZnO nanocrystals embedded in the nanoshells were also reduced till 1.5 nm, which induced the increase of the disorder degree of the nanoshell lattice. The controlling mechanism was discussed according to the competition of capping protection and the oxidation reaction of laser-induced plasma. Blue photoluminescence from the ZnO nanoshells was observed. The emission band exhibited abnormal red−blue shift and narrowing with increasing temperature. Such temperature-dependent behaviors can be well described by a localization model involving an interstitial zinc defect center. These results indicate that this method provides a convenient and universal way to obtain various metal/oxide core/shell nanoparticles with controllable microstructure, and it will be beneficial to an understanding of the physical origins of the blue emission in nanostructured ZnO as well as to extending its optical and electronic applications.

1. Introduction

As an important wide-band gap semiconductor, wurtzite ZnO with a band gap energy of 3.37 eV at room temperature and exciton binding energy of 60 meV possesses many important applications in electronic and optical devices,[1,2] especially in optoelectronic applications such as the UV/blue lasing media.[3] Therefore, the controlled synthesis of various ZnO nanostructures, such as nanocrystals, nanowires, nanobelts, and other complex nanoarchitectures,[4−7] has been extensively explored. Due to the important influence of the microstructure, such as core/shell structure, lattice ordering, intrinsic defects, and doping, on the properties and applications of semiconductor nanostructures,[8−11] the controlling of the microstructure is of great significance for the properties and applications, but seldom has such an investigation been reported from this consideration in the mass literature. On the other hand, some of the basic properties of ZnO are still unclear, especially for the dominant intrinsic defects[12] and the origins[13,14] of the defect-related visible emissions, which have continued to be controversial for several decades. In the photoluminescence (PL) of ZnO, typically there are emission bands in the ultraviolet (UV) and visible regions.[13−16] The UV emission is usually attributed to the interband transition or the exciton combination in ZnO.[15] Although the emissions in the visible region are usually considered to be associated with the intrinsic or extrinsic defects in ZnO, there still exist extensive controversies on the clearly related defect centers, and the unambiguous electron transition pathways are still unknown in detail.[14] Most researchers related the commonly observed green emission to a singly ionized oxygen vacancy.[16] As for the blue and violet PL in ZnO, they are comparatively unwonted, there are some reports about the violet PL (especially in ZnO films), but few about the blue emissions.[17,18] Moreover, the emergence of blue emissions exhibits considerable randomicity and uncontrollability in the reported results. This leads to great limitations in the studies of their features and mechanisms, and in the potential applications in short-wavelength electro-optical nanodevices, such as violet- or blue-light emitters.

Laser ablation in liquid medium (LAL) is of particular interest in view of its highly nonequilibrium processing character, which allows synthesis of novel metastable phases of materials and hardly possible synthesized materials by ordinary methods.[19,20] Recently, this method was applied to the synthesis of various metal,[21−24] oxide, and hydroxide nanostructures.[25−29] In this paper, we explore the rational control of the microstructure of Zn/ZnO core/shell nanoparticles. The results demonstrate that it could be realized through adjusting the applied surfactant concentration and laser power based on their effects on the competition of capping protection and oxidation reaction, indicating a convenient and universal way to obtain various metal oxide core/shell nanoparticles with controllable microstructures. Such ZnO nanoshells could be used as the model material for the study of the features and origins of the unwonted blue PL in nanostructured ZnO. Here, we further report the anomalous temperature-dependent behaviors of the blue PL in the ZnO nanoshells, and we try to explain that such behaviors may be associated with the localized state ensemble from the interstitial zinc defects in ZnO induced by LAL. This work will be beneficial in the exploration of the microstructure control method for the nanostructures by LAL and in understanding the physical origins of the blue emission in nanostructured ZnO, as well as in extending the related optical and electronic applications.

* Authors to whom correspondence should be addressed.
† E-mail: hbzeng@issp.ac.cn.
‡ E-mail: wpcai@issp.ac.cn.

10.1021/jp0770413 CCC: $37.00
Published on Web 12/04/2007

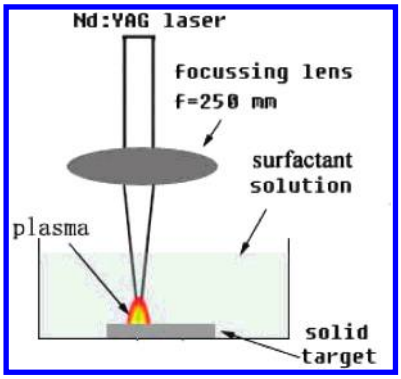

Figure 1. Schematic illustration of laser ablation in liquid (LAL).

2. Experimental Section

The laser ablation of a metal target[25−29] was performed in an aqueous solution with sodium dodecyl sulfate (SDS), according to the scheme illustrated in Figure 1. Briefly, a zinc plate (99.99%) was fixed on a bracket in a glass vessel filled with 10 mL of 0.05 M SDS (99.5%) aqueous solution, which was continuously stirred. The plate was located at a distance of 4 mm from the solution surface in the solution, and then it was ablated for 30 min by the first harmonic of a Nd:YAG pulsed laser (wavelength 1064 nm, frequency 10 Hz, pulse duration 10 ns) with the powers from 35 to 100 mJ/pulse, and the spot size about 2 mm in diameter. After ablation, all of the colloidal suspensions were centrifuged at 14000 rpm. Then, the obtained products or powders were rinsed several times with ethanol to remove the covered surfactant and dried at room temperature. For transmission electronic microscopy (TEM, JEM-200CX) and high-resolution TEM (HRTEM, JEOL-2010) examination, the power samples were redispersed in ethanol, then a droplet of the solution was placed on a carbon-coated copper grid. The characterizations with X-ray diffraction (XRD, the Philips X'Pert using the Cu Kα line 0.15419 nm) and X-ray photoelectron spectra (XPS, ESCALAB MK, adjusted using the C 1s line at 285.0 eV) were conducted directly for the power samples. Raman spectra were measured for the powder samples at room temperature on a Renishaw 1000 Raman spectroscope excited by a 514.5 nm laser. The PL spectra were measured with an Edinburgh luminescence spectrometer (FLS 920) with Xe lamp excitation at different temperatures and measured using a HeCd laser excitation source (325 nm).

3. Results and Discussion

3.1. Microstructure Control of Zn/ZnO Core/Shell Nanoparticles. In the LAL process illustrated in Figure 1, the high-temperature and high-pressure zinc plasma is first produced in the solid−liquid interface quickly after the interaction between a pulsed laser and the metal target. After that, the subsequent ultrasonic and adiabatic expansion of the hot zinc plasma leads to cooling of the zinc plume region and hence formation of zinc clusters.[29] After that, with the extinguishment of the plasma, the formed zinc clusters encounter the solvent and surfactant molecules in the solution, which induces some chemical reactions and capping effects. The final structure of the particles is closely dependent on the effect of applied SDS concentration and laser power on the competition between aqueous oxidation and SDS protection, according to the following three formulas:

$$Zn_{(target)} \xrightarrow{laser} Zn_{(plasma)}^{+} + 2e^{-} \quad (1)$$

$$Zn_{(plasma)}^{+} + 2e^{-} \rightarrow Zn_{(cluster)} \quad (2)$$

$$Zn_{(cluster)} + 2H_2O \rightarrow Zn(OH)_2 + H_2\uparrow \rightarrow ZnO + 2H_2O \quad (3)$$

According to this formation process, the final nanoparticles are the results of the competition between aqueous oxidation and SDS protection, which is greatly affected by the SDS concentration and laser power. So, the control of the microstructure of the obtained nanoparticles could be achieved by adjusting these parameters.

Figure 2presents the XRD pattern evolution with SDS. When the concentration of SDS was less than the critical micelle concentration (cmc) of SDS (0.0008 M), the products were mainly composed of wurtzite ZnO. However, when the SDS concentration was larger than the cmc, diffraction peaks corresponding to the metal Zn crystal increased and gradually dominated the patterns, together with decreasing ZnO peaks. Such XRD evolution indicated the possible changes in the composition and structure of the products.

Figure 3, parts A and B, shows the nanoparticles formed by LAL at the cmc and 70 mJ/pulse. It can be seen that the diameter of the spherical particles is in the range from about 10 to 50 nm. Besides these, the arrows point out the typical core/shell-structured nanoparticles (the detailed microstructure is presented later). According to the TEM statistics, the percentage of core/shell particles in end samples increased with SDS concentration, especially above the cmc, as presented in Figure 3C. This was co-incident with the above XRD evolution and demonstrated the conversion from pure ZnO nanoparticles to Zn/ZnO core/shell nanoparticles with SDS concentration increasing.

In order to further control the microstructure of the Zn/ZnO core/shell nanoparticles, the surfactant concentration was set at a constant of 0.05 M, and then the applied laser power was adjusted from high power to near threshold (here, the value is about 30 mJ/pulse). Figure 4A shows the typical TEM image of the product at a concentration of 0.05 M and laser power of 70 mJ/pulse, presenting well dispersed nanoparticles with 20 nm average diameter. Compared with Figure 3, parts A and B, the size of the nanoparticles further decreased, and the size distribution changed in a much narrower range with SDS concentration increasing. Most importantly, the laser power dependence of the shell thickness was very obvious from the HRTEM examinations in Figure 4, parts B−E. It can be found that the thickness of the ZnO shell was sharply reduced from 12 to 2.5 nm with the decrease of the laser power from 100 to 35 mJ/pulse. These results indicated good control of the shell thickness by laser power.

Subsequent XPS evolution provided further confirmation for the shell thickness control in a large quantity. For the pure ZnO nanocrystal (by 70 mJ/pulse and 0.0001 M SDS), the binding energy of Zn $2p_{3/2}$ was measured at 1022.2 eV (see Figure 5A). However, for the Zn/ZnO nanoparticles with a 6 nm shell (by 70 mJ/pulse and 0.05 M SDS), besides the Zn $2p_{3/2}$ peak corresponding to Zn^{2+} at 1022.1 eV, a broad peak with a higher energy tail was observed at 1024.1 eV, indicating the existence of Zn^0 in the sample (see Figure 5B).[30−32] This meant that ZnO was the predominant surface phase with a small amount of metal Zn in the sample. As the thickness of the shell decreased to 2.5 nm (by 35 mJ/pulse and 0.05 M SDS), the XPS peak corresponding to Zn^{2+} (1022.1 eV) decreased, but that corresponding to Zn^0 (1023.3 eV) increased in Figure 5C, which indicated that the main surface phase had changed into metal Zn. In a word, with the decrease of laser power, the dominant surface phase changed from ZnO to Zn. So, it could be deduced that the shell thickness decreased with applied laser power,

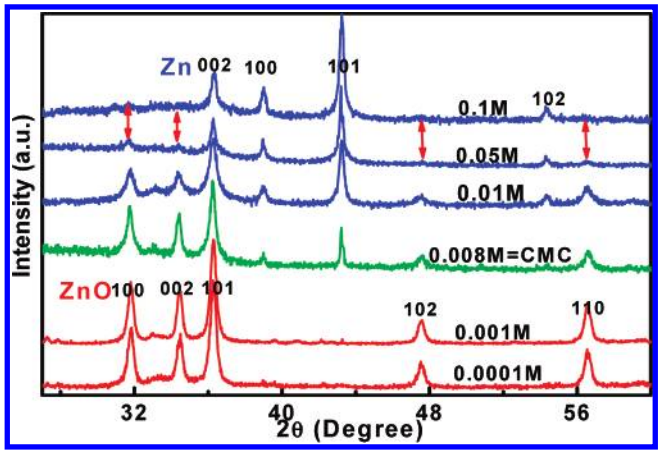

Figure 2. XRD pattern evolution of products with SDS concentration (laser power was fixed at 70 mJ/pulse).

which agreed well with the above HRTEM observations. The clear relation between the shell thickness and applied laser power is presented in Figure 5 D, exhibiting a monotone corresponding relation. So, this method provided us a convenient way to control the shell thickness of such core/shell nanoparticles just by adjusting the applied laser power.

Furthermore, the lattice microstructure evolution of the ZnO nanoshell with the applied laser power is presented in Figure 6. The three local magnified images were formed from the ZnO shells of core/shell nanoparticles by laser power of 70, 50, and 35 mJ/pulse (0.05 M SDS), respectively. It can be seen that the ZnO shells were composed of many fine nanocrystals, as well as a great deal of disorderly arranged areas and the boundaries among these nanocrystals. With the laser power decreased (same with the shell thickness), the nanocrystals in the shells became fewer in quantity. The disorder area enlarged, especially in nanoshells by very low power (see Figure 6C). On the other hand, the diameter of ultrafine ZnO nanocrystals embedded in the nanoshells was also reduced till 1.5 nm, which induced the increase of the disorder degree of the nanoshell lattice. Obviously, such disorder degree variance could be adjusted to some extent by the applied laser power in the LAL process and would affect a lot of properties of the nanomaterials.

As described above, the formation of nanparticles by LAL was the result of competition between aqueous oxidation and surfactant protection of Zn clusters produced in the high-temperature and high-pressure zinc plasma. The SDS concentration determined the content and speed of the surface adsorption of DS^- ions, and hence the extent of the protection effect to the zinc clusters. However, the applied laser power directly determined the intensity, density, and lifetime of the high-temperature and high-pressure zinc plasma, which not only affected the formation of the primal zinc clusters, but also the subsequent oxidation effect due to the correlative thermal effect. On this basis, the control mechanism is well illustrated in Figure 7. First, the high-temperature and high-pressure zinc plasma mainly composed of Zn atoms and Zn ions is produced in the solid−liquid interface quickly after the interaction between the pulsed laser and the metal target, as shown in Figure 7I. After that, the subsequent ultrasonic- and adiabatic-expansion of the hot zinc plasma results in the cooling of the zinc plume and hence rapid formation of zinc clusters. Then, with the extinguishment of the plasma, the formed zinc clusters encounter the solvent and surfactant molecules in the solution, which induces the occurrence of chemical reactions and capping effects, resulting in the competition between aqueous oxidation and SDS protection, as shown in Figure 7II. In order to summarize the different effects of the parameters on such competition, the final structure of the particles is dependent on the applied SDS concentration and laser power, as shown in Figure 7III.

As to the change from pure ZnO to Zn/ZnO core/shell nanoparticles with SDS, when SDS concentration was very low (C < cmc), the aqueous oxidation effect would be dominant (eq 3), leading to the pure ZnO nanoparticles. However, when C > cmc, the SDS molecules would form bilayer and even surface micelles onto the particle surface, and the protection of SDS became dominant, which would significantly decrease oxidation rate and result in the formation of Zn/ZnO core/shell nanoparticles. If the concentration of SDS was fixed, the ability of the surfactant protection could be taken as invariable. With a decrease of laser power, the density and intensity of the hot plasma would be diminished, which would induce the formation of fewer zinc clusters and particles (eqs 1 and 2), and greatly depress the laser-induced thermal effect. These would lead to the reduction of the particle diameter and the oxide shell thickness with the applied laser power decreasing.

In fact, in the LAL process, the highly nonequilibrium feature of the ultra-rapid reactive quenching of hot plasma plays an important role, especially for the microstructure, which includes the high-temperature and high-pressure extreme conditions and ultra-rapid reactive quenching within a single laser pulse.[19,20,29,35,36] Such extreme conditions in a confined space enables the formation of various defects that greatly deviate from the equilibrium process, making the species at a highly excited state, and lead the defect formation energy to be no longer an obstacle. Such a nonequilibrium process and conditions result in the emergence of abundant disorderly arranged atoms in the interfaces when the ultrafine nanocrystals are formed in the shells. Finally, when the applied laser power decreases, the disorder degree of shells will become more intensive due to the more rapidly quenching and more incomplete oxidization reaction. These are well confirmed by the microstructure observation in Figure 4.

There results demonstrate that, through parameters adjusting, LAL can be used to obtain a series of metal/oxide core/shell nanoparticles with controlled shell thickness and disorder degree. Such microstructure control would be expected to greatly affect some physical and chemical properties of nanomaterials, even obtaining nanostructures with novel functions.

3.2. Temperature-Dependent PL from the ZnO Nanoshells. Figure 8presents the corresponding RT-PL and PL excitation (PLE) spectra. Under the optimal excitation at 380 nm, a strong blue emission with a center at 445 nm was observed, in contrast to the previously reported violet or blue luminescence in ZnO nanostructures and films, which were usually very broad, weak, and of low signal-to-noise ratio.[17,18] Moreover, it should be noticed that such emission only covered the blue region, and there was almost no luminescence in the usual green-yellow region under such excitation, which would be obviously beneficial to its future application in short-wavelength electro-optical nanodevices. As mentioned above, such strong blue emission in nanostructured ZnO was very unwonted and its study was very limited.[17,18] The inset shows the PL emission with a center at 430 nm under the 325 nm laser excitation, whose difference should originate from the difference in excitation wavelength and excitation power in these two conditions.

In order to further explore the features of this blue emission, temperature-dependent PL measurements were conducted from 8 to 300 K, as shown in Figure 9. With the measurement temperature increasing, in addition to the decrease in intensity

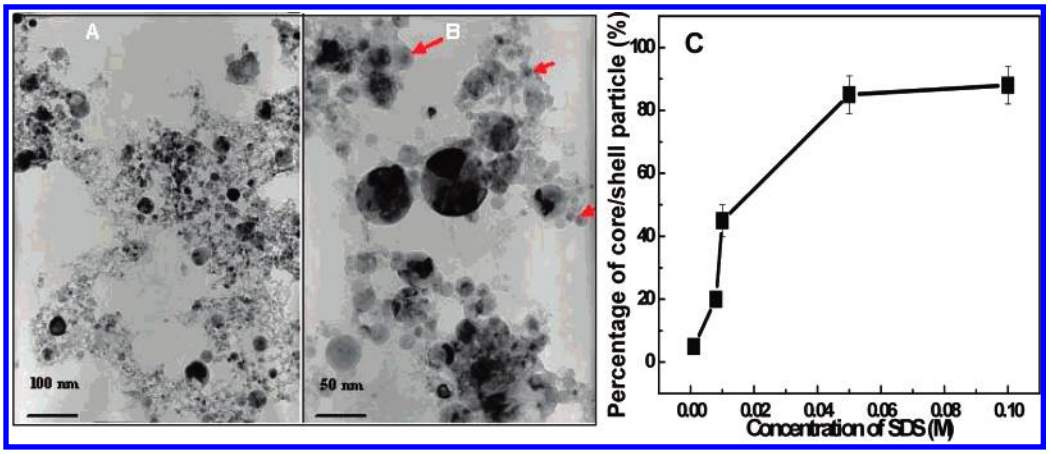

Figure 3. (A and B) TEM images of nanoparticles by 0.0008 M SDS (cmc) and 70 mJ/pulse, arrows point out the core/shell nanoparticles (the detailed microstructure characterization is presented later); (C) percentage evolution of core/shell particles with SDS concentration (by more than 500 particles statistics from TEM images).

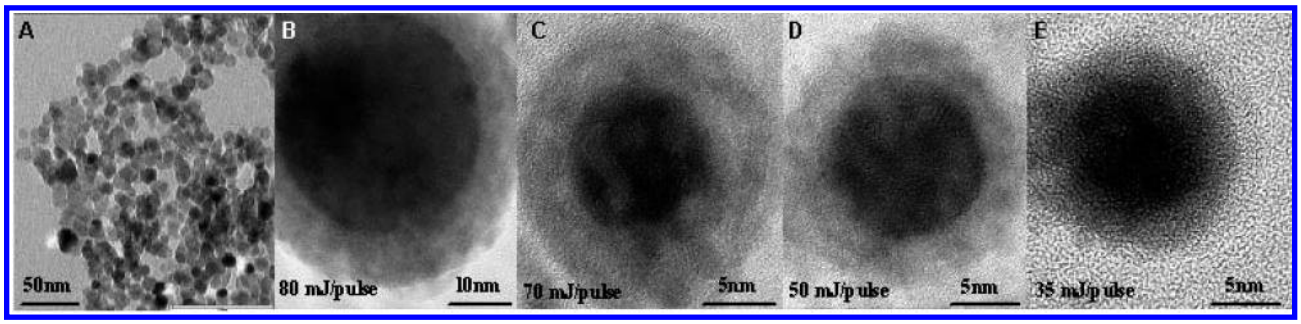

Figure 4. (A) Typical TEM image of nanoparticles by 0.05 M SDS and 70 mJ/pulse; (B−E) single-particle HRTEM images, showing shell thickness evolution with applied laser power. SDS concentration is fixed at 0.05 M.

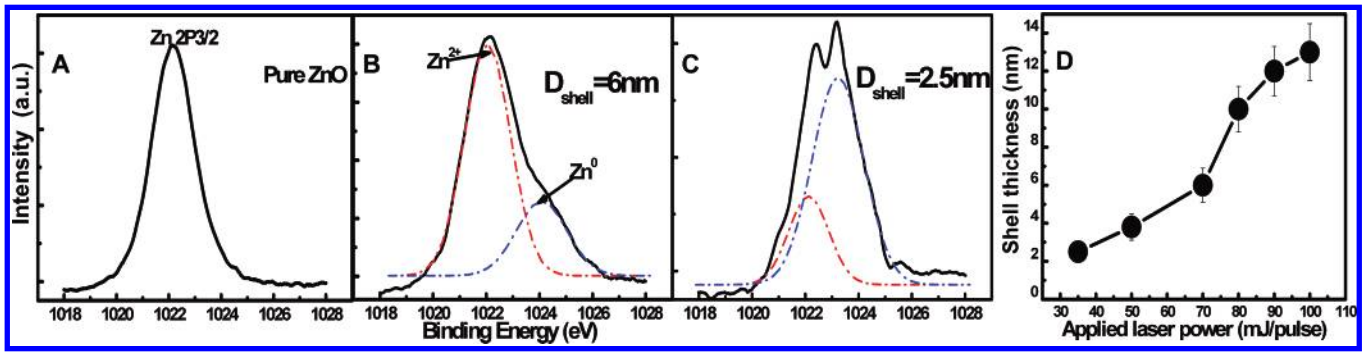

Figure 5. XPS evolution of nanoparticles with shell thickness: (A) pure ZnO nanoparticles (as reference) by 0.0001 M SDS and 70 mJ/pulse; (B) 6 nm-shell nanoparticles by 0.05 M SDS and 35 mJ/pulse; (C) 2.5 nm-shell nanoparticles by 0.05 M SDS and 70 mJ/pulse; (D) shell thickness vs applied laser power (more than 50 nanoparticles were considered for each sample).

(which was normal), the emission band shifted in an abnormal way of red first and then blue. The emission peak sharply red-shifted (at about 1.5 meV/K rate) first from 2.86 to 2.72 eV (140 meV totally) with an increase of the temperature from 8 to130 K, and then blue-shifted back to 2.75 eV from 130 to 300 K (30 meV in total), as seen in curve a of Figure 10. The temperature-dependent behavior for this blue emission was quite different from that of the reported UV and green emissions in common nanostructured ZnO, which showed a monotonous red- or blue-shift.[37,38]

In our previous work,[36] we had revealed that the blue emission was strongly related to the interstitial zinc in the ZnO, on the basis of coincidence of the peak energy with the theoretical prediction, the correlation between the anneal-induced PL evolution and change of the electron paramagnetic resonance *g* factor, and the LAL-induced instant local extreme conditions. Here, we focused on the temperature-dependent PL evolution of the blue emission from the ZnO nanoshells.

Generally, the temperature-dependent band gap E_g in semiconductor materials can be well described by the Varshni empirical formula:[39]

$$E_g(T) = E_g(0) - \alpha T^2/(\Theta + T) \quad (4)$$

where α is the Varshni parameter, Θ is the Debye temperature of the material, T is the absolute temperature, and $E_g(0)$ is the band gap when $T = 0$ K. For a perfect semiconductor, this formula predicts the monotonous shrinkage of band gap with an increase in temperature. Curve b in Figure 10 shows the corresponding result of ZnO according to eq 4 by setting α and Θ as 7.5×10^{-4} eV/K rate and 500 K,[38] respectively, exhibiting slow and monotonous decrease of $E_g(T)$ with rising temperature. This is in contrast to our experimental results (see curves a and b in Figure 10), which exhibit a much sharper decrease in the initial stage (at about 1.5 meV/K rate) and subsequent increase. Such great differences strongly imply that this blue emission is

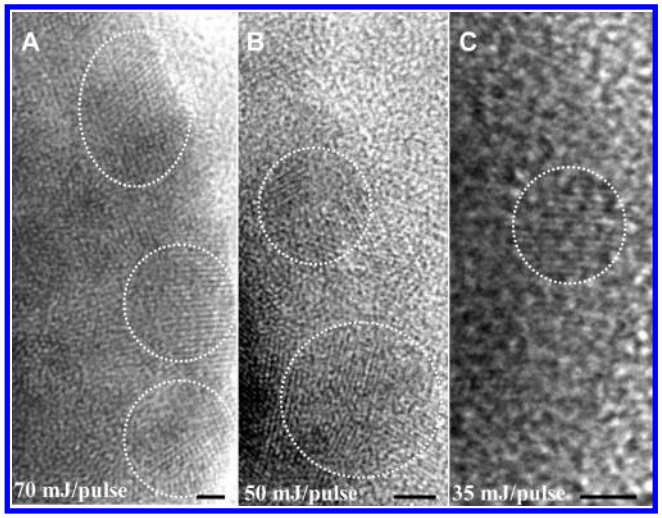

Figure 6. Local magnified HRTEM images of the ZnO shell, showing shell lattice evolution with applied laser power: (A) by 70 mJ/pulse; (B) by 50 mJ/pulse; (C) by 35 mJ/pulse. SDS concentration is fixed at 0.05 M. The inset circles denote the nanocrystals in the shells. The scale bar is 2 nm.

of different origin from the interband transition, and that, in addition to the normal band gap shrinkage, another certain stronger effects predominate in the temperature-dependent behaviors.

Recently, some anomalous temperature dependences of the luminescence peak position have been frequently observed in some semiconductors, such as InGaN, AlGaN, and GaInNAs quantum dots and wells.[39−42] A typical one of these phenomena is the red−blue shift of peak energy with temperature, which has been known to be related to the carriers' localization effect due to the doping or microstructure disorder-induced potential energy fluctuations.[39−43] In our case, there existed a high concentration of interstitial zinc in the ZnO nanoshells, which were discussed previously.[36] Such defects will inevitably induce lattice distortion surrounding the interstitial centers, and hence the potential energy fluctuation and then the interstitial zinc localized state levels, which was also very similar to the disorder-induced potential energy fluctuation in semiconductor alloys.[39−43] On this basis, the anomalous temperature dependence in this study could be described by the localization effect induced by the interstitial zinc defect centers.

At sufficiently low temperatures, the electrons will become trapped in the local minima, called carriers "freeze-out" since k_BT is smaller than the potential fluctuation amplitudes (barriers). With the temperature increasing, the electrons will gain sufficient thermal energy to overcome such potential barriers and become trapped, in turn, in the adjacent lower localized levels before their radiation transition, resulting in the sharp decrease of the emission energy. Obviously, the redshift of 140 meV from 8 to 130 K, in addition to the contribution of the band gap shrinkage 20 meV from eq 4, is just induced by such thermal redistribution of localized electrons. However, increasing temperature will also lead to reduction of the carrier lifetime. So when the temperature is high enough (>130 K here), the lifetime becomes dominant and an increase of the temperature will induce the electron transition at higher localized energy states due to the decreasing carrier lifetime with temperature increasing.

Quantitatively, on the basis of the assumption that the localized electronic states are a distribution function of energy in Gaussian-type Li and co-workers had presented a localization mode,[40−43] in which the distribution function of the localized states can be denoted as the following,

$$N(E,T) \propto \frac{e^{-(E-E_0)^2/2\sigma^2}}{e^{(E-E_a)/k_BT} + \tau_{tr}/\tau_r} \tag{5}$$

where $N(E,T)$ is the distribution of the localized carriers, E_0 is the statistic expectation value (or average value) of the localized state levels, E_a represents the barrier that the carriers must overcome to transfer (quasi-Fermi level in the localized state ensemble), k_B is the Boltzmann constant, and σ is the measurement (or standard deviation) of the energy distribution width for the localized electronic state. τ_{tr} and τ_r are the carrier transfer time and the carrier recombination time, respectively. Let $\partial N(E,T)/\partial E = 0$, the temperature-dependent peak position $E(T)$ equation can be derived as the following eqs 6 and 7. $x(T)$ is the temperature-dependent dimensionless coefficient.

$$E(T) = E_0 - \alpha T^2/(\Theta + T) - xk_BT \tag{6}$$

$$xe^x = \left(\frac{\tau_r}{\tau_{tr}}\right)\left[\left(\frac{\sigma}{k_BT}\right)^2 - x\right]e^{(E_0-E_a)/k_BT} \tag{7}$$

The blue emission in this study shows an abnormal red−blue shift with temperature, which is very similar to that in the semiconductor alloys with obvious localization effect, such as InGaN, AlGaN, and GaInNAs.[39−42] Similarly, this anomalous temperature dependence can be well interpreted by expanding the localization model to the interstitial zinc defect centers. Lin and co-workers[44] have calculated that the energy gap from the interstitial zinc level to the valence band is about 2.9 eV, which is consistent with the previously reported interstitial zinc level of 0.22 eV below the conduction band edge by Kroger and Bylander,[45,46] and very close to the energy range of the blue emissions in this study also, and hence can be considered as the center value E_0 of the distribution function of the localized electronic states.

We can thus fit the experimental results of peak position evolution with temperature (shown in curve a of Figure 10) by eqs 6 and 7. The corresponding result is shown in curve c of Figure 10 by taking $E_0 = 2.9$ eV, $\sigma = 50$ meV, and $\tau_{tr}/\tau_r = 0.022$ ps/500 ps,[15,38,42] respectively. The parameter $E_a - E_0$ is thus determined to be 100 meV. Quite good agreement of the fitting and experiment results is obtained (see curves a and c in Figure 10), which means that the abnormal temperature-dependent behaviors of the blue emission are mainly attributed to the localization effect of the interstitial zinc defect centers in ZnO.

Further, in the localization mode, the barrier height $E_a - E_0$ reflects the magnitude of the carrier localization effect, and the obtained value 100 meV in this fitting is obviously larger than those in reported semiconductor alloys (typically, 75 meV for InGaN epilayer),[42] which indicates the strong localization effect for the blue emission. Moreover, the decreasing rate (about 1.5 meV/K) in the initial near-linear part of the peak position−temperature relation, induced by the thermal redistribution according the localization model, is also much larger than those in reported semiconductor alloys (typically, about 0.2 meV/K for InGaN epilayer),[42] which also demonstrate the strong localization effect.

In addition, this strong localization effect is further verified by the temperature-dependence of the PL width, which shows steps (not monotone lineshape), even slight narrowing, at the temperature range from 30 to 130 K, as shown in Figure 11A

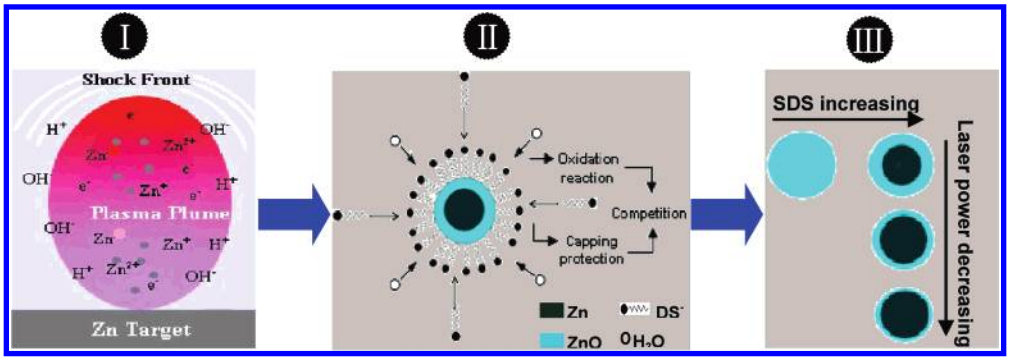

Figure 7. Schematic illustration of the microstructure controlling of nanoparticles by LAL: (I) laser-induced high-temperature and high-pressure plasma; (II) competition effect of capping protection and oxidation reaction; (III) structure evolution with SDS concentration and laser power.

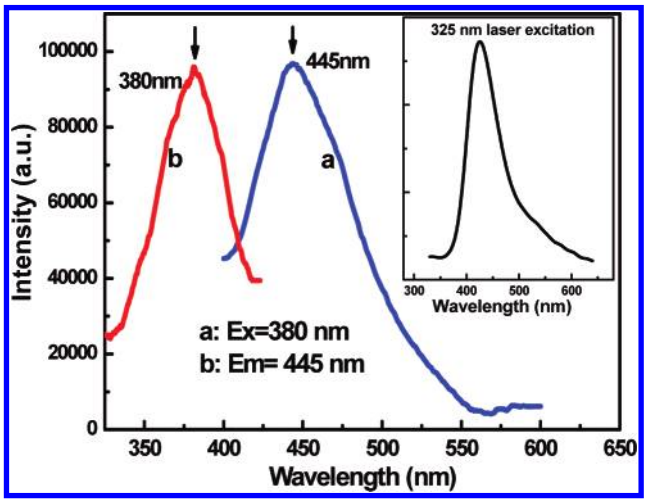

Figure 8. (a) RT-PL (excited at 380 nm) and (b) excitation spectra (emitting at 445 nm) of as-prepared nanoparticles by LAL with 0.05 M SDS and 70 mJ/pulse. The insert is PL emission under 325 nm laser excitation.

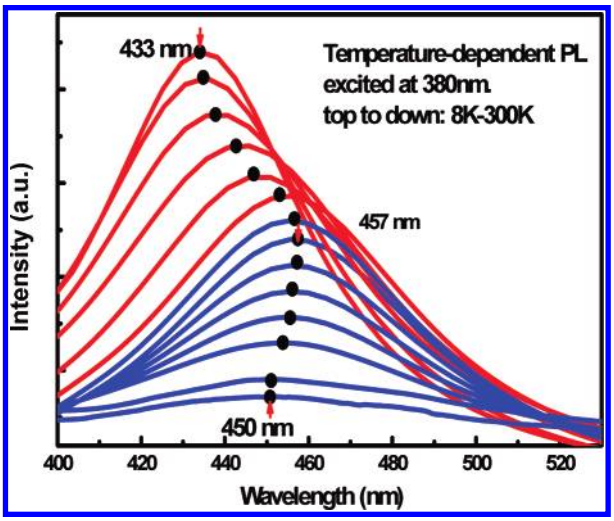

Figure 9. Temperature-dependent PL spectra of Zn/ZnO core/shell nanoparticles from 8 to 300 K at 380 nm excitation.

in the measured spectra. Such abnormal narrowing is agreeable to the calculated distribution functions from eq 5 in the localized model, as shown in Figure 11B. The red-shift of the peak energy and the narrowing of the fwhm with temperature can be clearly seen just in the temperature range, which is co-incident with the experiment observation of the abnormal narrowing. Furthermore, the line shape of the distribution functions exhibits unusual variation with an increase of temperature (for example, comparing the calculated curve at 70 K with that at 130 K). It

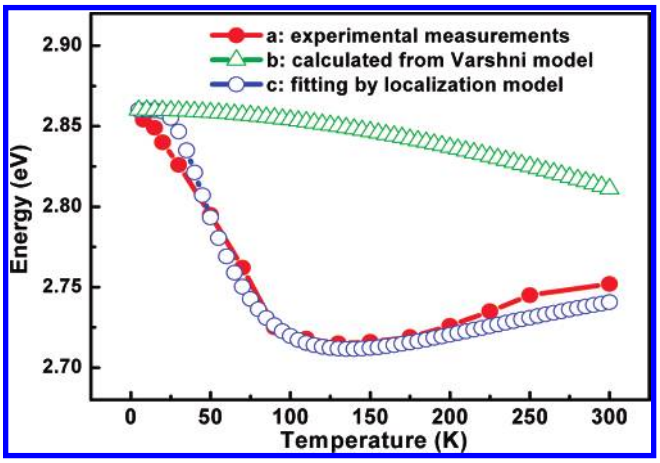

Figure 10. Peak energy vs temperature from (a) above experimental measurements, (b) the Varshni model fitting, and (c) the localization model fitting.

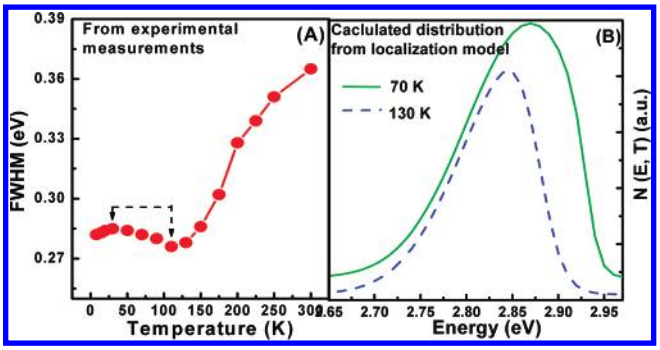

Figure 11. Temperature-dependent fwhm (A) obtained from the above measurements and calculated up-converted carrier distribution function (B) from the localization model.

can be noticed that the decrease at the high-energy side is more rapid than that at the low-energy side. Therefore, the distribution of the localized states becomes more asymmetric and narrow as the temperature increases in this range. This can just be explained as a result of carrier thermal transfer from the localized states to the adjacent localized states at lower energy. On the other hand, it should be noticed that these temperatures are just in the range with thermal redistribution of localized electrons described above.

Such a strong localization effect is strongly related to the great disorder degree of the local microstructure induced by the interstitial zinc, which will lead to the large potential energy fluctuations. As we know, the interstitial-type defect can cause a greater lattice distortion than other point defects, such as vacancies and substitute atoms. In addition, as previously reported,[36] LAL-induced instant local extreme conditions can

lead to the high nonequilibrium of the growth process, which results in the "freezing" of highly concentrated interstitial zinc in the ZnO lattice of the nanoshell. These are very similar to that in the reported semiconductor alloys to produce potential energy fluctuations,[39−42] and hence the strong localization effect. The abnormal red−blue temperature dependence of the blue PL of the ZnO nanoshell is just the result of such a strong localization effect, and it is strongly related to the high microstructure disorder degree. At the same time, these phenomena further confirm the interstitial zinc-related origin for such blue PL of the ZnO nanoshell.

4. Conclusions

In summary, this paper demonstrates that the microstructure of the Zn/ZnO core/shell nanoparticles synthesized by laser ablation in liquid can be facilely controlled by adjusting the applied surfactant concentration and laser power. With SDS concentration over cmc, the nanoparticles change from pure ZnO to a Zn/ZnO core/shell structure. Further, with a decrease of the applied laser power, the ZnO shell thickness decreases until 2.5 nm, whereas the disorder degree increases. The controlling mechanism was attributed to the highly nonequilibrium feature of the ultra-rapid reactive quenching process and the effects of SDS and laser power parameters. The blue PL from the ZnO nanoshells shows an abnormal red-shift first and then a blue-shift with temperature increasing from 8 to 300 K. Good agreement between experiment and localization model fitting were obtained on the temperature dependence of emitting energy and peak width. Such temperature dependence of the blue emission is attributed to the strong localization effect from the interstitial zinc atoms in the ZnO lattice of the nanoshells due to the extreme process of LAL. It is the interstitial defects that induce the local potential energy fluctuation and then the interstitial zinc localized state levels. The localization of the up-converted carriers plays a key role in the radiative recombination producing such blue PL. This work indicates that laser ablation in the liquid method provides a convenient and universal way to obtain various metal/oxide core/shell nanoparticles with controllable microstructure, and it will be beneficial to final clarification of the physical origins of blue emissions in nanostructured ZnO and to extending its optical and electronic applications.

Acknowledgment. This project is financially supported by the National Natural Science Foundation of China (Grant Nos. 10604055, 50271069) and National Project for Basic Research (Grant No. 2005CB623603).

References and Notes

(1) Dai, Z. R.; Pan, Z. W.; Wang, Z. L. *Adv. Funct. Mater.* **2003**, *13*, 9.
(2) Wong, E. M.; Searson, P. C. *Appl. Phys. Lett.* **1997**, *4*, 2939.
(3) Lau, S. P.; Yang, H. Y.; Yu, S. F.; Yuen, C.; Leong, Eunice, S. P.; Li, H. D.; Hng, H. H. *Small* **2005**, *10*, 956.
(4) Cao, B.; Teng, X.; Heo, S. H.; Li, Y.; Cho, S. O.; Li, G.; Cai, W. *J. Phys. Chem. C* **2007**, *111*, 2470.
(5) Li, L.; Pan, S.; Dou, X.; Zhu, Y.; Huang, X.; Yang, Y.; Li, G.; Zhang, L. *J. Phys. Chem. C* **2007**, *111*, 7288−7291.
(6) Shen, G. Z.; Bando, Y.; Lee, C. J. *J. Phys. Chem. B* **2005**, *109*, 10779.
(7) Mo, M. S.; Yu, Jimmy, C.; Zhang, L. Z.; Li, S. A. *Adv. Mater.* **2005**, *17*, 756.
(8) Yu, K.; Zaman, B.; Romanova, S.; Wang, D. S.; Ripmeester, J. A. *Small* **2005**, *3*, 332.
(9) Ding, Y.; Gao, P. X.; Wang, Z. L. *J. Am. Chem. Soc.* **2004**, *126*, 2066.
(10) Mahan, G. D. *J. Appl. Phys.* **1983**, *54* (7), 3825.
(11) Radovanovic, P. V.; Norberg, N. S.; McNally, K. E.; Gamelin, D. R. *J. Am. Chem. Soc.* **2002**, *124*, 15192.
(12) Zhang, S. B.; Wei, S. H.; Zunger, A. *Phys. Rev. B* **2001**, *63*, 075205.
(13) Cao, B. Q.; Cai, W. P.; Zeng, H. B. *Appl. Phys. Lett.* **2006**, *88*, 161101.
(14) Djurišić, A. B.; Leung, Y. H.; Tam, K. H.; Ding, L.; Ge, W. K.; Chen, H. Y.; Gwo, S. *Appl. Phys. Lett.* **2006**, *88*, 103107.
(15) Fallert, J.; Hauschild, R.: Stelzl, F.; Urban, A.; Wissinger, M.; Klingshirn, C.; Kalt, H. *J. Appl. Phys.* **2007**, *101*, 073506.
(16) Kohan, A. F.; Ceder, G.; Morgan, D.; Van de Walle, C. G. *Phys. Rev. B* **2000**, *61*, 15019.
(17) Wu, J. J.; Liu, S. C. *Adv. Mater.* **2002**, *14*, 215.
(18) Wang, Q. P.; Zhang, D. H.; Xue, Z. Y.; Hao, X. T. *Appl. Surf. Sci.* **2002**, *201*, 123.
(19) Patil, P. P.; Phase, D. M.; Kulkarni, S. A.; Ghaisas, S. V.; Kulkarni, S. K.; Kanetkar, S. M.; Ogale, S. B.; Bhide, V. G. *Phys. Rev. Lett.* **1987**, *58*, 238.
(20) Ogale, S. B.; Patil, P. P.; Phase, D. M.; Bhandarkar, Y. V.; Kulkarni, S. K.; Kulkarni, S.; Bhide, V. G.; Guha, S. *Phys. Rev. B* **1987**, *36*, 8237.
(21) Mafune, F.; Kohno, J. Y.; Takeda, Y.; Kondow, T. *J. Phys. Chem. B* **2003**, *107*, 4218.
(22) Mafune, F.; Kohno, J. Y.; Takeda, Y.; Kondow, T. *J. Am. Chem. Soc.* **2003**, *125*, 1686.
(23) Sylvestre, J. P.; Kabashin, A. V.; Sacher, E.; Meunier, M.; Luong, J. H. I. *J. Am. Chem. Soc.* **2004**, *126*, 7176.
(24) Tsuji, T.; Kakita, T.; Tsuji, M. *Appl. Surf. Sci.* **2003**, *206*, 314.
(25) Huang, C. C.; Yeh, C. S.; Ho, C. J. *J. Phys. Chem. B* **2004**, *108*, 4940.
(26) Yang, L.; Way, P. W.; Yin, L.; Scott, T. B. *Nanotechnology* **2007**, *18*, 215602.
(27) Usui, H.; Shimizu, Y.; Sasaki, T.; Koshizaki, N. *J. Phys. Chem. B* **2005**, *109*, 120.
(28) Liang, C. H.; Shimizu, Y.; Masuda, M.; Sasaki, T.; Koshizaki, N. *Chem. Mater.* **2004**, *16*, 963.
(29) Zeng, H. B.; Cai, W. P.; Li, Y.; Hu, J. L.; Liu, P. S. *J. Phys. Chem. B* **2005**, *109*, 18260.
(30) Liu, B.; Zeng, H. C. *J. Am. Chem. Soc.* **2004**, *126*, 16744.
(31) Bae, S. Y.; Choi, H. C.; Na, C. W.; Park, J. *Appl. Phys. Lett.* **2005**, *86*, 033102.
(32) Futsuhara, M.; Yoshioka, K.; Takai, O. *Thin Solid Films* **1998**, *317*, 322.
(33) Saito, K.; Sakka, T.; Ogata, Y. *J. Appl. Phys.* **2003**, *94*, 5530.
(34) Sakka, T.; Iwanaga, S.; Ogata, Y. H.; Matsunawa, A.; Takemoto, T. *J. Chem. Phys.* **2000**, *112*, 8645.
(35) Usui, H. *J. Phys. Chem. C* **2007**, *111*, 9060.
(36) Zeng, H. B.; Cai, W. P.; Hu, J. L.; Duan, G. T.; Liu, P. S. *Appl. Phys. Lett.* **2006**, *88*, 171910.
(37) Varshni, Y. P. *Physica* **1967**, *34*, 149.
(38) Hamby, D. W.; Lucca, D. A.; Klopfstein, M. J.; Cantwell, G. *Appl. Phys. Lett.* **2003**, *93*, 3214.
(39) Eliseev, P. G.; Perlin, P.; Lee, J.; Osiński, M. *Appl. Phys. Lett.* **1997**, *71*, 569.
(40) Li, Q.; Xu, S. J.; Cheng, W. C.; Xie, M. H.; Tong, S. Y.; Che, C. M.; Yang, H. *Appl. Phys. Lett.* **2001**, *79*, 1810.
(41) Li, Q.; Xu, S. J.; Xie, M. H.; Tong, S. Y. *J. Phys.: Condens. Matter* **2005**, *17*, 4853.
(42) Xu, S. J.; Li, Q.; Dong, J. R.; Chua, S. J. *Appl. Phys. Lett.* **2004**, *84*, 2280.
(43) Grenouillet, L.; Bru-Chevallier, C.; Guillot, G.; Gilet, P.; Duvaut, P.; Vannuffel, C.; Million, A.; Chenevas-Paule, A. *Appl. Phys. Lett.* **2000**, *76*, 2241.
(44) Lin, B. X.; Fu, Z. X.; Jia, Y. B. *Appl. Phys. Lett.* **2001**, *79*, 943.
(45) Bylander, E. G. *J. Appl. Phys.* **1978**, *49* (3), 1188.
(46) Kroger, F. A. *The Chemistry of Imperfect Crystals*; North-Holland: Amsterdam, 1964; p 691.